“Older circuits get richer”: neurogenesis timeline shapes hubness and neurogenetic profiles of the adult human brain

I. Diez[1,2], F. Garcia-Moreno*[3,4,5], N. Carral-Sainz[6], S. Stramaglia[7], A. Nieto-Reyes[8], M. D’Amato[5,9,10], J.M. Cortes[5,11,12], P. Bonifazi[5,11]*

[1] Gordon Center for Medical Imaging, Department of Radiology, Massachusetts General Hospital, Harvard Medical School, Boston, MA, USA
[2] Athinoula A. Martinos Center for Biomedical Imaging, Department of Radiology, Massachusetts General Hospital, Harvard Medical School, Charlestown, MA, USA
[3]Achucarro Basque Center for Neuroscience, Scientific Park of the University of the Basque Country (UPV/EHU), Leioa, Spain.
[4]Department of Neuroscience, Faculty of Medicine and Odontology, UPV/EHU, Barrio Sarriena s/n, Leioa, Bizkaia, Spain.
[5] IKERBASQUE: The Basque Foundation for Science, Bilbao, Spain.
[6]Departamento de Ciencias de la Tierra y Física de la Materia Condensada, Facultad de Ciencias, Universidad de Cantabria, Santander, Spain
[7]Dipartimento Interateneo di Fisica, Università degli Studi di Bari Aldo
Moro, and INFN, Sezione di Bari, Italy
[8]Departamento de Matemáticas, Estadística y Computación, Facultad de Ciencias, Universidad de Cantabria, Santander, Spain
[9]Department of Medicine and Surgery, LUM University, Casamassima, Italy
[10]Gastrointestinal Genetics Lab, CIC bioGUNE - BRTA, Derio, Spain
[11]Computational Neuroimaging Lab, Biocruces-Bizkaia Health Research Institute, Barakaldo, Spain
[12]Department of Cell Biology and Histology, University of the Basque Country (UPV/EHU), Leioa, Spain
** The authors equally contributed*

ABSTRACT

Understanding the architectural principle that shapes the topology of the human connectome at its multiple spatial scales is a major challenge for systems neuroscience. This would provide key fundamental principles and a theory for browsing brain’s networks, to ultimately generate hypothesis and approach to which extent key structures might impact different brain pathologies. In this work, we propose the hypothesis that the centrality of the different brain nodes in the human connectome is a product of their embryogenic age, and accordingly, early-born nodes should display higher hubness, and viceversa for late-born nodes. We tested our hypothesis by identifying and segmenting eighteen macroregions with a well-known embryogenic age, over which we calculated nodes’ centrality in the structural and functional networks at different spatial resolutions. First, nodes’ structural centrality correlated with their embryogenic age, fully confirming our working hypothesis. However, at the functional level, distinct trends were found at different resolutions. Secondly, the difference in embryonic age between nodes inversely correlated with the probability of existence and the weights of the links. This indicated the presence of a temporal developmental gradient that shapes connectivity and where nodes connect more to nodes with a similar age. Finally, brain transcriptomic analysis revealed high association between embryonic age, structural-functional centrality and the expression of genes related to nervous system development, synapse regulation, and human neurological diseases. Overall, these results support the hypothesis that the embryogenic age of brain regions shapes

the topology of adult brain networks. Our results show two key principles, “preferential age attachment” and “older gets richer” on the wiring of the human brain, thus shedding new light on the relationship between brain development, transcriptomics, node centrality, and neurological diseases.

INTRODUCTION

The most characteristic anatomical property of brain networks is their organization at multiple spatial scales, which interconnect micro-scale cell-body neurons within local micro-circuit domains, scaling up to macro-scale levels where long-range connections allow centimetre-distant neurons and circuits to communicate[1,2]. The characteristic branching properties of neurons, the major cellular brain components, is what makes the structure of the brain unique as a network, when compared to other branch-structured organs characteristic of invertebrate and vertebrate species[3]. A key challenge for fundamental and clinical neuroscience is to decipher the rules of connectivity that shape brain networks in order to understand how the brain works and how traumatic or neurological injuries affect brain functionality[4].

The general structure and functionality of the human brain and its embedded connectivity are the result of its developmental history, which is at the same time the product of evolution[5]. This way, the brain follows developmental instructions that decisively impact on the diversification of neural connections and their functions. In particular, the developing human brain closely resembles the developing brains of other mammals and vertebrates[6]. In this context, the development and evolution of brain circuits are strictly related, so the oldest evolutionary circuits are also those that were embryogenically generated earlier[7]. Although previous studies have focused on the development of brain networks at different stages of maturation also in relation to the appearance of key network structures such as central nodes[8], there are still no detailed studies that fully relate the connectivity of the adult human brain with sequential (evolutionarily preserved) neurogenesis of circuits.

The structural organization of brain networks shapes how the brain dynamically operates by coordinated firing of neurons or neuronal ensembles across different spatio-temporal scales, ultimately leading to brain functions[1,2]. Thus, the structural organization of brain networks in the spatial domain has been mirrored into the concept of functional networks in the temporal domain[9,10]. Functional networks reflect the statistical relationship between the activity of different brain regions or neurons, based on the underlying assumption that when neurons or brain circuits are cooperatively active at the same time, they can engage in similar functions[9].

The complexity arising from both the anatomy and the dynamics of brain circuitry needs a general mathematical framework capable of quantifying and describing the interactions of structural and functional networks at multiple scales. In this context, complex networks emerged in the last two decades as a powerful mathematical framework for quantifying the very diverse properties of real-world networks from very different domains ranging from biology to sociology and beyond[11]. Notably, different

studies assessing real-world networks' data have shown small-world, scale-free or heavy-tailed distribution network organizations as stereotyped topologies in many distinct domains[12,13] . When applied in the context of neuroscience, these key topologies have been identified at the structural-functional level in microcircuits, meso- and macro-scale networks[14].

Complex networks also provided models underlying the formation of the above-described topologies[12]. Specifically, when looking to network development and how the different nodes make connections as a function of their actual connectivity degree, a pioneering study[15] by Barabasi and Albert showed that the principle "the rich gets richer" (a.k.a. "preferential attachment") led to the development of the scale-free networks, characterized by the presence of highly connected rare nodes or hubs. In this work, inspired by the Barabasi model[15], we aim to combine the heavy-tailed signatures widely observed in the brain networks' organization together with the stereotyped evolutionary-preserved sequential neurogenesis in the developing brain, to hypothesize that brain networks' topology could be shaped according to the rule that "older gets richer", i.e. evolutionary older circuits or early generated along embryogenesis, are the ones highly central in the adult brain network organization[16]. As a consequence, brain circuits' hubness quantified by metrics of complex networks' centrality should correlate with their embryogenic age. Our hypothesis is grounded and extrapolates at macro-scale previous pioneering evidence showing that at the micro-circuit level GABAergic neuronal hubs were functionally identified in the hippocampal circuits and also revealed as early born GABAergic neurons both in developing and adult murine circuits[17–19].

To test our hypothesis, we reviewed previous literature to obtain the time sequence for the earliest neurogenesis time of the different brain circuits and translated into the human brain by segmenting those circuits from magnetic resonance imaging (MRI). We first identified eighteen macro-circuits (MACs) according to their first (i.e. earliest) neurogenic time (FirsT, estimated in embryonic days) during embryogenesis. Since MACs' volumes span across multiple scales, we studied the brain networks with two different spatial resolutions: a low resolution parcellation corresponding to the eighteen MACs, and a high resolution parcellation composed of approximately two and half thousand regions of interest (ROI) of similar volumes.

Structural and functional brain networks were obtained using 7 Tesla MRI images acquired within the Human Connectome Project[20]. At high resolution level, we observed that FirsT reversely shaped the nodes' centrality in the structural and functional networks, where highly central nodes displayed respectively early and late FirsT. Distinctly, the structural and functional nodes' centrality of the low-resolution MACs similarly correlated with FirsT, with higher centrality displayed in the early born MACs. In addition, we observed that FirsT-lags reversely correlated with wiring probability and connection weight, so ROIs and MACs connected more and stronger with those at similar age. Finally, brain transcriptomic analysis revealed also high association between genes' expression, FirsT and nodes' centrality, in respect to physiological nervous system development and synapse regulation, and to neuropathological conditions. Notably, a

significant rate of genes involved in major neurological diseases such as epilepsy, Parkinson's, Alzheimers' and autism displays extreme correlation values with nodes' centrality (we especially mention high correlation for highly studied genes such as SCN1A, SNCA and APOE). The results provide a new multi-scale evidence on how neurogenesis time shapes structural and functional networks, brain nodes' centrality and their transcriptomics in patho-physiological conditions and underlie two main neurogenesis preferential wiring principles: "the older gets richer" and "preferential age attachment".

RESULTS

Segmentation of brain circuits according to neurogenesis time points: from brain networks to transcriptomics

Human brain circuits were differentiated and segmented according to their First neurogenic birth Time (FirsT), i.e. the post-conception day (or embryonic day) at which the first neurons of the circuit are generated (fig 1 A) and following the criteria established in methods. Our list organized human circuits according to FirsT, from older to younger circuits (table 1). We identified 18 macrocircuits (MACs) for which a timing sequence based on their FirsT could be provided. Other relevant circuits, for which detailed developmental information is known, such as the neocortical layers and thalamic nuclei, could not be segmented on MRI (see Supplementary Information).

We used resting-state fMRI and dMRI images acquired at 7 T within the Human Connectome project from N=184 healthy subjects to reconstruct the structural-functional brain networks (see fig. 1 B and Methods). Since the volume of the different MACs spanned more than two orders of magnitude (see Supplementary Fig. 1B), MACs were also parcellated (see Methods) to obtain spatially segregated ROIs with a volume comparable to the smallest circuits (like Locus Coeruleus), i.e. about several dozen of voxels each (see Supplementary Fig. 1A with overall ROI volume distribution). Each of the 18 MACs had a correspondent FirsT while for all ROIs obtained within a given MAC we assigned the same FirsT. The number of ROIs per MAC is reported in Table 1. A total of 2566 ROIs were defined in the brain. In order to explore the existence of possible patterns of correlation between FirsT and brain circuit connectivity at different spatial resolutions, centrality and segregation metrics were calculated for each ROI and MAC (fig. 1B). In addition, the transcriptomics of the different MACs were related to FirsT (Fig. 1C) to provide a complementary biological correlate of brain nodes related to neurogenesis.

Centrality vs neurogenesis in the structural - functional brain networks

To quantify the centrality of each ROI and MAC in the brain networks, we calculated from the adjacency matrices of the brain connectivity networks five different centrality metrics, specifically the node strength (NS), the eigenvector centrality (EC), the centrality of the subgraph (SC), average first-neighbour strength (AFNS), between-ness centrality (BC), and one segregation metric such as the clustering coefficient (CC; see Methods for the rationale for the choice of metric). These metrics were calculated on high spatial resolution networks composed of 2566 ROIs (referred to as high-resolution structural and functional connectivity networks, respectively SC^{HR} and FC^{HR}) and low spatial resolution networks composed of 18 MACs (referred to as low-resolution structural and functional connectivity, respectively SC^{LR} and FC^{LR}). The SC^{HR} and FC^{HR} were calculated from the average of all subjects, respectively, from probabilistic tractography and resting-state activity correlations (note that only positive functional links were considered, see Methods). The SC^{LR} and FC^{LR} were calculated as the average of the links connecting ROIs within the MAC pairs, in SC^{HR} and FC^{HR} respectively. Note that while the diagonal of the connectivity matrices (self-connections) was taken to be zero in the high-resolution space, in the low-resolution space it was not zero, and

represented the average of the links between the ROIs within a given MAC (internal MAC connectivity).

To test our main hypothesis that the structural centrality of brain nodes is inversely correlated with embryogenic day, such that the earlier, the higher the centrality, we computed Spearman's partial correlation (SP-pCorr, see Table 2) between the nodes' centrality (and segregation) and FirsT, eliminating the effect of the cofounder white matter volume per ROI or MAC, which also shows a gradient between early and late generated structures (Supplementary Fig. 2). Similarly, we repeated the same calculation for the functional networks, in this case removing the cofounder of gray matter volume per ROI or MAC (Supplementary Fig. 2). The results for the SCNs and FCNs are summarized in table 2 and in fig. 2A for both spatial resolutions.

When looking at high-resolution networks, the centrality of SC^{HR} and FC^{HR} nodes showed significant inverse trends with FirsT, respectively negative and positive correlations with absolute values greater than 0.26 for all centrality metrics (apart for the case of BC for which a poor correlation was observed below 0.15). Note that the negative correlations observed for SC^{HR} (physically constrained spatial domain) support the leading hypothesis that early born brain regions (such as the locus coeruleus and brainstem) have higher "hubness" or centrality (with strongest correlation value of -0.44 observed in the case of EC). On the contrary, in the case of the FC^{HR} (functional domain related to time and dynamics) the positive correlations between centrality and FirsT observed highlight the greater centrality of late brain circuits (such as neocortical ones). In relation to the segregation of nodes, the clustering coefficient showed a significant positive correlation with FirsT (SP-pCorr=0.33) only in the case of FC^{HR}.

For low-resolution networks, we observed negative centrality correlations with respect to FirsT in both SC^{LR} and FC^{LR}, with a clear inverse trend for the functional case relative to the high-resolution case. In the case of structural networks, the correlations for all centrality and segregation metrics had significant ($p<0.015$) values ranging between -0.58 (for the BC) and -0.81 (for the EC). In the case of functional networks, significant negative correlations were observed in 3 of 5 centrality metrics (specifically EC, SC and AFNS) with values ranging from -0.51 to -0.83, while the correlation for the NS was -0.47 at the limit of significance ($p=0.06$). Node segregation measured with the clustering coefficient showed a significant correlation with FirstT (SP-pCorr = -0.77) only in the case of SC^{LR}. The negative trend between the time of birth of the 18 different MACs and the eigenvector centrality of the SC^{LR} and FC^{LR} can be visualized on a brain surface respectively in fig. 3A.

Next, we checked if the difference in neurogenesis time (ΔFirsT) could also be related to the probability of existence and weight of the links (fig. 2B). In SC^{HR} and FC^{HR} respectively, where a connection is present in 5% and 45% of the overall node pairs, link probability decreased as a function of ΔFirsT with a Spearman correlation of -0.53 ($p<0.01$) and -0.49 ($p=0.01$), and similarly, link weight decreased with a correlation of -0.81 ($p<0.001$) and -0.93 ($p<0.001$). In the SC^{LR} and FC^{LR}, only the link weight was considered as these matrices are highly dense, which decreased as a function of ΔFirsT

with a correlation of -0.50 ($p<0.001$) and -0.43 ($p<0.001$). The link weights shown in supp. Fig. 3 and supp. Fig 4 for each MAC (where each plot is a given MAC and its FirsT is highlighted as a vertical broken line), allows to visualize how brain circuits generated at close neurogenic timepoints tend to connect more strongly.

The linear temporal visualization of the structural connectivity of three representative MACs, respectively with earliest (Locus Coeruleus, 28 days), latest (occipital cortex, FirsT 54 days) and intermediate (hippocampus, FirsT 40 days) FirsT is reported in fig. 3 B1-3. Such visualization shows that NS of the earliest MAC are much higher than later MACs and, for the case of the Locus Coeruleus, it also shows that brain circuits generated at close neurogenic timepoints are more strongly connected.

The transcriptomic of brain circuits according to FirsT. To find a potential list of genes associated with brain circuits' FirsT, brain networks' centrality and brain transcriptomics, data from the Allen Human Brain Atlas (AHBA) were used. Average Spearman correlations between genetic expression of 20,737 protein coding genes with FirsT, structural and functional connectivity centrality was computed (fig. 4A). First, gene expression correlation with functional centrality increased linearly in respect to FirsT (Pearson correlation 0.63, $p<0.01$) while an opposite trend was observed for the structural centrality (Pearson correlation -0.74, $p<0.01$). A lower anti-correlation (Pearson correlation -0.26, $p<0.01$) was observed for gene expression in functional and structural centrality maps. Secondly, 787 genes were found with a correlation >1.64 standard deviation from the obtained distribution ($r>0.44$). Gene set enrichment analysis of biological process showed that the genes were overrepresented for development of central nervous system and axons, cell morphogenesis involved in neuron differentiation and regulation of synaptic transmission, synaptic plasticity, synapse organization, cation transmembrane transport and neuron projection development (fig. 4B). Additionally, different cellular components were also overrepresented for neuronal cell body, component of synaptic and postsynaptic membrane, synaptic vesicle and glutamatergic synapse, dendrite, axon, voltage-gated potassium channel complex, perikaryon and growth cone (fig. 4B). A restricted list of genes with a correlation >1.96 standard deviation from the obtained distribution ($r>0.5237$) was also analyzed. The obtained 96 genes were overrepresented for nervous system development, synapses and anatomical structural morphogenesis Supplemetary fig. 5). The term-term network analysis with biological processes and cellular components show how different functional annotations are related. A highly connected group of annotations related to brain and neuron projection development, central nervous system differentiation and synapse organization was found. Also, another group of annotations related to dendrites, axons, modulation of chemical synaptic transmission and trans-synaptic signalling is clearly defined. This group of annotations is highly connected with cation channel complex, regulation of ion transport and system processes and adenylate cyclase-modulating G protein-coupled receptor signalling pathway (fig. 4C).

We finally tested the hypothesis that genetic contribution to neurological diseases is related to brain networks' centrality maps. Therefore, we studied the distribution of correlation between gene expression and structural-functional networks' centrality (we refer to this as gex-centrality distribution), expecting genes that have been causally related to neurological disorders to show higher absolute values of correlations (fig. 5). In particular, we focused on Autism Spectrum Disorder (ASD), Parkinson's disease (PD), Alzheimer's disease (AD) and epilepsy, and considered two main human gene datasets (see Methods), GeneCards (www.genecards.org) and the Genome-Wide Association Study Catalog (GWAS Catalog; https://www.ebi.ac.uk/gwas/): for each gene and disease, these provide respectively a relevance score (based on the amount of reported literature linking a gene to a disease; black dots in fig. 5 A) and statistical evidence of their causal relation to risk of disease (via GWAS data; red dots in fig. 5A, and fig. 5B). As shown in Figure 5B, genes associated to neurological diseases (via GWAS) were not evenly spread across the gex-centrality distribution and showed a significant enrichment at its percentile tails (see black arrows in fig. 5B), thus supporting our hypothesis. Of note, typifying this observation were genes with a well-known role such as *APOE, TREM2 and SORL1* (Alzheimer's disease), *SCN1A* and *CPLX1* (epilepsy) and *SNCA* and *MAPT* (Parkinson's disease), *KCTD1252* and *PARD3B53* (Autism Spectrum Disorder) among others.

DISCUSSION

In this work, we use the earliest neurogenesis time (FirsT) reported for brain circuits to study adult brain networks reconstructed from structural-functional (resting-state) MRI with low (MAC level) and high (ROI level) spatial resolution. By correlating centrality metrics of complex networks with FirsT, we observe a decreasing gradient of structural hubness in MACs and ROIs from earlier to later genesis. This observation confirms our main working hypothesis that "older nodes get richer" in hubness within brain networks. In the functional domain, the centrality of the MACs follows the same trend, while, on the contrary, the ROIs structurally developed later show a higher centrality. Note that when going from a high spatial scale (ROI; 2566 nodes) to a low spatial scale (MAC; 18 nodes), internal connectivity within MACs is discarded, and this lack of connectivity may be especially relevant when assessing the centrality measurements on larger circuits like the neocortical ones.

Our results are in agreement with the logic behind the differences of early and late developmental brains. Early generated neurons in the human brain mature into a favourable environment for cell growth, migration and axonal pathfinding. Late neurons, on the other hand, differentiate into a stiffer neuropil, full of extracellular matrix, their growth and axonal pathfinding are therefore restricted by the logic of developmental maturation. In addition, the growth of the brain itself plays a significant role into the formation of long-range connectivity. Whereas the brain at four gestional weeks (GW; when Locus Coeruleus neurons start their genesis), extends 3-5 mm, the human fetal brain at eight GW (when many cortical neurons are generated) measures 27-31mm[21]. The formation of the general structural connectivity is impacted by the timing of neurogenesis.

The “older gets richer” rule matches well previous literature on the connectomics of birth-dated populations, both for neuronal populations that we were able to trace at the MRI as well as for other smaller regions of the brain, not visible in MRI. Amongst the first neurons appearing in the brain are those in the Locus Coerules[22–25] (LC) and motor neurons of brainstem and midbrain, including the trigeminal mesencephalic nucleus[26]. These organize in small nuclei, and although most of them cannot be segmented by MRI (in our case we only considered the LC and Raphe nuclei), our model predicts they all are potentially highly relevant at connectivity level. Noradrenergic LC neurons establish connections that span the whole brain[27], and both LC and trigeminal nuclei contribute to pathologies such as Alzheimer when are degenerated[28–30].

Away from the brain stem, pioneering studies on GABAergic hub cells[17] on developing murine hippocampus have been showing how indeed early born GABAergic neurons represent operationally and morphologically hub cells[18,31], later also identified in other structures[32] and in the adult murine hippocampus[19]. Within the neocortex, where different neuronal populations are generated at sequential neurogenic stages[33], but where these birth-dated circuits cannot be tracked by MRI, hubs are related to neurogenesis. A recent computational study of neocortical circuits reported that

targeted-injuries on the layer-five hub-neurons was producing the greatest damage to the structural functional integrity of neocortical circuits[34]. Layer 5 neurons are amongst the earliest generated in the neocortex. More widely, early neuronal types, in hippocampus, cortex, brain stem and mesencephalon, might display a hub role due to their early neurogenesis. As an example, stimulation of Purkinje cells in the cerebellum, i.e. an early born GABAergic neuronal type in an early born circuit, has been shown to inhibit spontaneous hippocampal seizures in a mouse model of temporal lobe epilepsy[35].

Regarding the topology of brain networks, we observe a decreasing gradient of the probability and strength of connections, as a function of neurogenesis time differences, both in structural and functional networks at a high and low level of spatial resolution. Therefore, nodes generated close in time showed a higher probability and strength of connections. This latter observation supports the hypothesis that brain networks follow a "preferential age attachment rule" in which nodes are more likely to connect if their neurogenesis age difference is smaller. From the biological point of view, this might explain why neurons establish their major connections during a short temporal window of plasticity, namely critical period[36,37], before getting functional and mature. Therefore, neurons of equivalent birthdate tend to share these permissive temporal windows, which allows their mutual/reciprocal connection. The rules of "preferential age attachment" and "older gets richer" extrapolate to the context of brain networks the pioneering model of Barabasi-Albert on the construction of scale-free networks and the genesis of network hubs.

Brain connectivity, as any other biological feature, is ruled and limited by natural selection. Due to the intimate relationship between development and evolution, it is likely that the rules that relate neurogenic time to connectivity patterns are conserved amongst species. Indeed, previous studies on the development of brain networks in the worm *C. elegans* proved the early appearance of neuronal hubs[38]. Moreover, neurons linked by long-range connections tend to be generated at around the same neurogenic time and early on[38], reinforcing the concept of a plastic temporal window around neuronal birthdate. Ultimately, all connections are evolutionary shaped to optimize axonal-length and speed of connections[39,40]. Similarly to our results, other vertebrate brains are likely governed by the same rules of development and connectivity. Indeed, brain regions shown here to have the greatest hubness are deeply conserved in the vertebrate brain[41], suggesting their crucial importance for all vertebrates. These regions include the posterior regions of the brain, such as the brain stem and mesencephalon, and the cerebellum, which are known to be relatively similar across the vertebrate taxa[42]. In part, the rule of the older gets richer suggests that ancient circuits -such as those in brainstem, related to autonomic animal functions and directly involved in the survival of the animal- are more influential in the network and more stable in evolution. As a crucial example, it has been recently demonstrated the deeply conserved neurogenic formation of the cerebellum in several species of vertebrates[43], and its remarkable orchestrating hub role to impact epileptic brain dynamics[35]. On the other side of the spectrum, circuits related to associative tasks -more related to cognition and

human-specific behaviour- are not necessarily conserved, appear later in neurogenesis. We showed that in high-resolution networks how their structural hubness (low) is inversely related to their functional one (high).

In relation to brain transcriptomics, we have studied how spatial maps of gene expression in adult brains correlate with FirstT and structural-functional centrality maps. We have found that genes whose expression correlates positively with the centrality of structural circuits tend to show higher expression in the first generated circuits. In contrast, genes whose expression is anti-correlated with the centrality of structural circuits show higher expression in circuits with late neurogenesis. Vice versa is observed for functional networks. Thus, the transcriptomics of structural and functional networks appears to be differentially driven by genes whose expression is developmentally regulated. Previous studies have investigated the genetic basis of human brain network structure and function with converging evidence that anatomical connectivity is more strongly shaped by genetics compared to functional connectivity (see[44] for a review). In our study, we add that the developmental sequence (specifically the first neurogenic time) as an additional key variable to interpret genetics in relation to the connectome, providing a key criterion to link embryogenesis to the topology of adult brain networks. It also sheds light onto the longitudinal reconstruction of developing brain networks which present key technical challenges[8].

To test if genes with a known role in neurological diseases are tightly linked with network centrality -so having a potential key impact on network hubs- we studied the correlation between network centrality maps and the expression of genes associated to epilepsy, autism, Parkinson disease and Alzheimer's disease, which overall represent models of neurodevelopmental and neurodegenerative models. We found top contribution for two genes well-known to drive PD, such as *SNCA*[45,46], encoding the parkinsonism-associated Lewy body protein alpha synuclein, and *MAPT*[47], encoding the microtubule-associated protein tau. Altogether, our results show that in nodes with higher structural centrality *SNCA* and *MAPT* are expressed at lower levels in physiological conditions (see Supplementary Table and Fig. 5A1). We also found top associations for the *APOE*, which codes for apolipoprotein E and is directly related to AD, cerebral amyloid angiopathy, PD and other neurological diseases[48], and *TREM2*, a receptor expressed in myeloid cells 2 and related to microglial biology, high risk of developing AD[49] and prion diseases[50]. In addition, the *SORL1* gene, encoding the sortilin-related receptor and previously associated with early and late-onset Alzheimer's disease[51], was also found in the upper percentile with a high positive correlation with functional centrality. For the case of the ASD, also a higher number of genes from the GWAS dataset were observed in the first five percentile of functional centrality distribution (see supp. Table), out of them we highlight *KCTD12*[52] and *PARD3B*[53]. For epilepsy, we highlight the presence of the *SCN1A* gene, which codes for the Alpha 1 Subunit of the Sodium Voltage-Activated Channel, occupying position 36 in correlation with the functional centrality of 20,787 genes considered, and causally related to Dravet Syndrome, a rare genetic disease causing one of the most devastating forms of childhood generalized epilepsy[54].

Based on data from four different neurological conditions, our results provide broader and idiopathic support for the hypothesis that neurological disease may be linked to key topological alterations of brain networks in relation to node hubness[55]. Thus, altered transcriptomics of genes whose expression correlates highly with network centrality could lead to profound neurological lesions and disease. In this context, stroke and other brain circuitry damage to early-generated structures (such as those in the brainstem region) are known to have life-threatening consequences compared with later-generated cortical structural damage.

METHODS

Neurogenesis timeline of brain circuits

We hypothesize that the strength of adult connectivity for a given region depends on its developmental time. For the selection of the circuits under investigation, we needed to reach a compromise between the conflicting resolution level of MRI and the developmental structural units. Certainly, there are hundreds of brain structures and circuits that can be segmented from MRI (cf. the list of areas that were identified in the AAL classification[56] and others[57]), although many of these regions do not develop independently (e.g. the many neocortical areas). In contrast, there are brain regions that are developmentally relevant but cannot be precisely segmented by MRI (e.g. thalamic nuclei). Therefore, we followed two criteria to select the list of brain circuits that were ultimately studied: developmental independence and MRI segmentability.

Developmental independence: Based on how the brain is generated during embryonic formation, we chose brain regions that developed from independent units of the early differentiated brain, called fundamental morphogenic units (FMU[58]). Early in development, all vertebrate brains display several brain vesicles: telencephalon, diencephalon, midbrain, and hindbrain. Each of these vesicles is segmented into several neuromeres, which are developmentally independent rings of the neural tube that form the major regions of the brain. Each neuromere comprises several FMUs along its dorsal-ventral axis (figure 1A). Within a given FMU, neurogenesis forms most of the neurons of its derivative. As an example, the m1 neuromere in the mesencephalon gives rise to most of the neurons in the superior colliculus, so we consider the superior colliculus to be a developmental unit. The available literature shows the specific date of birth of the different populations of each development unit (see below).

MRI segmentability: The human brain evolved following an unprecedented expansion of the neocortex, which develops from a single developmental unit[59]. But this expansion has come at the expense of shrinking many brain regions, some so small that they cannot be segmented at MRI resolution. For example, within the rombencephalon that generates the brainstem and pons, there are up to 11 rhombomeres, each of which hosting a number of FMUs but, none of them can be segmented with MRI. Thus, we consistently identified segmentable brain structures from MRIs. As a consequence, no circuit was assigned to two different dates of birth. Most brain structures were generated during a neurogenic period, but only the first day after conception in which neurons began to appear in a circuit was considered the first neurogenic time (FirsT). Most of the brain structures were generated during a neurogenic period, but only the earliest post-conception day at which neurons began to appear in a circuit was considered the time of interest, which we call the first neurogenic time (FirsT).

MRI DATASET AND PROCESSING

Participants

Neuroimaging data was acquired by the Human Connectome Project, WU-Minn Consortium (Principal Investigators: David Van Essen and Kamil Ugurbil;

1U54MH091657) funded by the 16 National Institutes of Health (NIH) Institutes and Centers that support the NIH Blueprint for Neuroscience Research; and by the McDonnell Center for Systems Neuroscience at Washington University. For this study, we took N = 184 healthy subjects acquired at 7 Tesla (72 males; 112 females; 24 participants between 22-25 years; 84 between 26-30 years; 73 between 31-35; and 2 of them with more than 36). High-resolution structural T1 images, functional magnetic resonance images at rest (fMRI) and diffusion tensor images (DTI) were used. For more information on the acquisition parameters, see Supplementary Methods and the Human Connectome Project documentation (http://www.humanconnectome.org/).

Image preprocessing

Minimal pre-processed data was downloaded from Human Connectome[60]. T1 structural images were aligned to anterior and posterior commissures, skull stripped, corrected for gradient distortion and bias field, and the non-linear transformation to MNI152 standard space was computed. Using a one-step resampling approach, resting state functional data was corrected for gradient-non-linearity-induced distortion, movement within runs with a rigid body transformation (six parameters linear transformation) and EPI distortion. Both the transformation from reference image to structural T1 image and T1 to standard space were also used in the one-step resampling approach. A subject specific functional data projected to MNI152 was obtained. Diffusion images were normalized for b0 intensity, EPI distortion, movement and eddy currents were corrected, and gradient nonlinearities were corrected. B0 image was coregistered to subject anatomical T1 images. For more details on the minimal preprocessing of the human connectome refer to the original paper[60]. To further reduce the noise in functional data a general linear model was used for removing linear and quadratic trends, the contribution of motion, cerebrospinal fluid and white matter signals. Additionally, a band-pass filtering (0.01–0.08 Hz) and spatial smoothing with an isotropic Gaussian kernel of 6-mm FWHM was applied.

Brain macrocircuits (MACs) at low resolution

Several regions from different brain MRI atlases were combined to generate 18 different macrocircuits. The atlases included Automated Anatomical Labeling (AAL[56]), Freesurfers Desikan-killiany atlas[61], CIT168 subcortical atlas[62] and locus coeruleus atlas[63]. For locus coeruleus and raphe nuclei were chosen as the functional ROIs englobating them. For further details see Table 1.

Brain regions of interest (ROIs) at high resolution

A high resolution parcellation was generated after clustering the functional data to study network properties with about 2,500 ROIs. In particular, and similar to[64], the clustering was performed based on temporal correlations between pairwise voxel time series imposing a constrain to ensure spatially contiguous ROIs. This was performed in two stages: 1. Clustering at the single subject level, and 2. A second clustering applied to individual subject data. To avoid ROIs with voxels belonging to several circuits rather than performing clustering on the whole brain this strategy was applied separately for

each circuit. Small circuits were neglected, and those voxels inserted into the nearest circuit. After parcellation, we took all ROIs overlapping with some of the existing circuits, resulting in 2,566 regions covering the whole brain.

STRUCTURAL AND FUNCTIONAL BRAIN NETWORKS

High-resolution

After image processing, the connectivity matrices were obtained at high-resolution, representing two modalities structural and functional networks composed by 2566 ROIs. Individual subject functional connectivity matrices were obtained by averaging all the time series of the voxels belonging to each generated ROI, and by calculating the Pearson correlation value between the time series corresponding to each pair of ROIs. The average of the functional matrices across all subjects was then calculated, and all links with negative weights were set to zero, thus ignoring negative correlations. This final matrix defined the high-resolution functional connectivity matrix (FC^{HR}).

FSL functions were used to quantify the individual subject structural connectivity matrices. First FSL BEDPOSTX was used to model crossing fibers, and subsequently the probabilistic tractography was performed with PROBTRACKX to generate a #ROI × #ROI matrix per subject. Matrices were normalized between 0 and 1 dividing each element by their maximum. The average across subjects' matrices was finally obtained, and only the top 5% of higher weights were considered to create the high-resolution structural connectivity matrix (SC^{HR}), in agreement with previous studies[65]. For both functional and structural matrices, the principal diagonal elements were set to zero to avoid ROI self-connectivity interactions.

Low-resolution

Given a pair of macro-circuits MAC_i and MAC_j (with $i \neq j$), and the two sets of ROIs belonging to them $R_i=\{ROI_{i1}, \dots, ROI_{iN}\}$ and $R_j=\{ROI_{j1}, \dots, ROI_{iM}\}$, where N and M are their respective number of ROIs, the average of all functional links in FC^{HR} connecting the two sets was defining the low-resolution functional connectivity matrix (FC^{LR}), accounting for the functional link between MAC_i and MAC_j, i.e.:

$$FC_{ij}^{LR} = \frac{1}{N * M} \sum_{a \in R_i} \sum_{b \in R_j} FC_{ab}^{HR}$$

Notice that for FC^{LR} the principal diagonal has non-zero elements, representing the internal connectivity within a given MAC, i.e.,

$$FC_{ii}^{LR} = \frac{1}{N * (N-1)} \sum_{a \in R_i} \sum_{b \in R_i} FC_{ab}^{HR}$$

Similarly, we built the low-resolution structural connectivity matrix (SC^{LR}), where the MACs' volumes (V_i and V_j) where now used for normalization, i.e.:

$$SC_{ij}^{LR} = \frac{1}{V_i \times V_j} \sum_{a \in R_i} \sum_{b \in R_j} SC_{ab}^{HR}$$

and for diagonal elements:

$$SC_{ij}^{LR} = \frac{1}{V_i^2} \sum_{a \in R_i} \sum_{b \in R_i} SC_{ab}^{HR}$$

For the calculation of MAC_i volume V, we summed the volumes of the corresponding ROIs (set R_i) expressed as number of voxels.

COMPLEX NETWORKS ANALYSIS

By construction, all networks analysed were symmetric and weighted, with non-negative values. We used MATLAB (Mathworks) to run different metrics implemented in the Brain Connectivity Toolbox (*https://sites.google.com/site/bctnet/measures/list*). In particular, we calculated Node Strength, Eigenvector Centrality, Subgraph Centrality, Betweenness Centrality and Clustering Coefficient. We analysed four types of connectivity matrices, a sparse one with high number of nodes (SC^{HR}, 2566 nodes and 5% connectivity), a dense one with high number of nodes (FC^{HR}, 2566 nodes and 45% connectivity), and nearly-fully connected matrix with a small number of nodes (SC^{R} 18 nodes, >95% connectivity) and a fully connected matrix with a small number of nodes (FC^{LR} 18 nodes, 100% connectivity). In order to use the same metrics across all networks considered, we discarded the node degree (being this not meaningful in fully connected conditions), the flow coefficient (being this not applicable in fully connected conditions), the local efficiency (diverging computational time in dense conditions and high number of nodes) and Pagerank Centrality (being this a variant of the eigenvector centrality). Moreover, we also implemented the Average of First-Neighbour Connectivity (AFNC). Given an adjacency matrix A of size NxN, and the Nodes' Strengths (NS_i, $i=1, \dots, N$), $AFNS_i$ for each node is calculated as:

$$AFNS_i = \frac{1}{N-1} \sum_{j \neq i}^{N} A_{ij} * NS_j$$

To remove the potential bias introduced by ROIS with higher white or grey matter influence, for each individual partial volume estimates of white matter and grey matter were estimated using FSL FAST tool[66]. For each functional ROI the average white and grey matter partial volume estimates from the group average were computed. We used Spearman partial correlation to calculate the correlation between structural (functional) centrality and FirsT while regressing out white (grey) matter partial volume estimates per ROI or per MACs (considering the average across the ROIs within eachj MAC), in the case of low- and high-resolution networks respectively.

The difference in neurogenesis time between two ROIs or MACs was defined as ΔFirsT. In regard to the average connection probability and weight between nodes as function

of difference in neurogenesis time ΔFirsT (see fig. 2), the matrix representing ΔFirsT for pairs of ROIs ($\Delta FirsT^{HR}$) was first computed according to:

$$\Delta FirsT_{ab}^{HR} = FirsT_a - FirsT_b$$

where *(a,b)* is pair of ROIs . Similarly, it was calculated the matrix for the low-resolution networks' case for pairs of MACs ($\Delta FirsT^{LR}$). Note that by construction $\Delta FirsT^{HR}$ and $\Delta FirsT^{LR}$ are antisymmetric. In the case of the high-resolution networks, the Spearman correlation of connection probability and average link weight as function of ΔFirsT was calculated only considering non-negative elements of $\Delta FirsT^{HR}$ and the correspondents' elements in the SC^{HR} (FC^{HR}; note that the same results would be obtained for the non-positive case). Being *F* the set of elements in the matrix satisfying the condition $\Delta FirsT^{HR}$=D (with 0<=D<=max(ΔFirsT)=26 days), the structural (functional) connection probability for ΔFirsT=D was calculated as the fraction of existent links out of the set F in the adjacency matrix SC^{HR} (FC^{HR}). Similarly, for the same ΔFirsT=D and set F, the average link weight was calculated from the adjacency matrix SC^{HR} (FC^{HR}) on the existent links. In the low-resolution case, since SC^{LR} and FC^{LR} are not sparse matrix and have a connectivity density above 95%, only the link weight was calculated as function of ΔFirsT. Similarly to the high-resolution networks' case, the Spearman correlation between the links' weights and ΔFirsT was calculated on the non-negative links of the SC^{LR} (FC^{LR}) and the correspondent elements in ($\Delta FirsT^{LR}$).

GENETIC FINGERPRINT OF BIRTHDATE CIRCUITS

To investigate genetic fingerprints of birthday circuits, we used the transcriptome dataset from Allen Human Brain Atlas[67,68]. The AHBA provides whole-brain genome-wide expression values for 20,737 protein-coding genes extracted from 3,702 brain samples spatially distributed throughout the brain of six human post-mortem brains. Using brain sample information, brain maps representing the spatial distribution of each gene in the 18 circuits was generated based on recent recommendations[69,70]: i) expression values from multiple probes were averaged; ii) each sample was mapped to one of the 18 circuits atlas. Samples falling outside were mapped to the nearest circuit, if this was closer than 3mm; iii) for each individual, median expression values across all samples mapped to the same circuit were calculated; iv) a group expression map was computed by calculating the mean of the expression values of the six individual donors. This approach was repeated to generate another expression atlas containing 90 brain regions based on the 68 cortical regions of the Desikan-Killiany atlas, 16 subcortical regions from freesurfer, cerebellum, brain stem, locus coeruleus and dorsal raphe nucleus. This 90 regions' atlas was used to asses genetic associations of structural and functional organization of the brain.

To search the underlying genetic fingerprints of both microcircuit EED and brain functional and structural eigenvector centrality a combined score for each of the 20,737 protein-coding genes was computed.

$$r(g) = \frac{r_{EED,18}(g) - r_{SCC,90}(g) + r_{FCEC,90}(g)}{3}$$

The score r for a given gene g is the average Spearman correlation between the expression of gene g with EED in 18 regions $r_{EED,18}(g)$, with structural connectivity centrality in 90 regions $r_{SCC,90}(g)$ and with functional connectivity centrality in 90 regions $r_{FCC,90}(g)$. The sign of the spearman correlation of structural connectivity was inverted as it follow and inverse pattern compared to EED and functional connectivity. Genes with a score >1.64 standard deviation from the obtained distribution were used for further analyses (r>0.4389; 787 genes).

An overrepresentation analysis was computed to find common functional annotations in the obtained gene list. Gene set enrichment was computed for biological processes and cellular component annotations from Gene Ontology using PANTHER13.1 (http://www.pantherdb.org/) and Fisher's exact test with FDR correction to perform the statistical testing (p value < 0.05). Additionally, Metascape[71] was used to construct an annotation-to-annotation network. Terms with a p-value < 0.01, a minimum count of 3, and an enrichment factor > 1.5 were grouped into clusters based on their membership similarities. P-values were calculated based on the accumulative hypergeometric distribution, and q-values using the Banjamini-Hochberg procedure to account for multiple testings. Kappa scores were used as the similarity metric when performing hierachical clustering on the enriched terms, and sub-trees with a similarity of > 0.3 were considered being a cluster. The most statistically significant term within a cluster was chosen to represent the cluster name. To capture the relationships between the terms the survived enrichment terms were rendered as a network plot, where terms with a similarity > 0.3 were connected by edges. The terms in clusters with a q < 0.005 were chosen, with the constraint that there are no more than 15 terms per cluster and no more than 250 terms in total. The network was visualized using Cytoscape[72], where each node represents an enriched term and is colored first by its cluster ID.

In relation to genetics and neurological diseases, the full gene lists related to Epilepsy, Autism, Parkinson's and Alzheimer's disease have been downloaded from www.genecards.org and https://www.ebi.ac.uk/gwas/ (GWAS). In the case of the Genecards database, the relevance score has been included in our study. For a detailed definition of relevance score in relation to a disease see https://www.genecards.org/Guide/Search.

The analysis of distribution of the genes from the GWAS Catalog has been performed in interval of five percentiles. Enrichment for GWAS Catalog genes in the outermost percentiles vs the rest of the distribution has been tested via binomial distribution.

In relation to fig. 5, the lists of genes from the Genecards and from the GWAS list with a correlation >1.64 standard deviation (see vertical black broken lines in fig. 5 A) are reported as supplementary tables, with information on structural and functional correlation (value, rank and percentile), and relevance score (value, rank and percentile).

REFERENCES

1. Betzel, R. F. & Bassett, D. S. Multi-scale brain networks. *NeuroImage* **160**, 73–83 (2017).

2. Buzsáki, G. *Rhythms of the brain*. (Oxford University Press, 2006).

3. Ochoa-Espinosa, A. & Affolter, M. Branching Morphogenesis: From Cells to Organs and Back. *Cold Spring Harbor Perspectives in Biology* **4**, a008243–a008243 (2012).

4. Fox, M. D. Mapping Symptoms to Brain Networks with the Human Connectome. *N Engl J Med* **379**, 2237–2245 (2018).

5. Cisek, P. & Hayden, B. Y. Neuroscience needs evolution. *Phil. Trans. R. Soc. B* **377**, 20200518 (2022).

6. Workman, A. D., Charvet, C. J., Clancy, B., Darlington, R. B. & Finlay, B. L. Modeling Transformations of Neurodevelopmental Sequences across Mammalian Species. *Journal of Neuroscience* **33**, 7368–7383 (2013).

7. Abzhanov, A. von Baer's law for the ages: lost and found principles of developmental evolution. *Trends in Genetics* **29**, 712–722 (2013).

8. Oldham, S. & Fornito, A. The development of brain network hubs. *Developmental Cognitive Neuroscience* **36**, 100607 (2019).

9. Friston, K. J. Functional and effective connectivity in neuroimaging: A synthesis. *Hum. Brain Mapp.* **2**, 56–78 (1994).

10. Feldt, S., Bonifazi, P. & Cossart, R. Dissecting functional connectivity of neuronal microcircuits: experimental and theoretical insights. *Trends in Neurosciences* **34**, 225–236 (2011).

11. Boccaletti, S., Latora, V., Moreno, Y., Chavez, M. & Hwang, D. Complex networks: Structure and dynamics. *Physics Reports* **424**, 175–308 (2006).

12. Cimini, G. *et al.* The statistical physics of real-world networks. *Nat Rev Phys* **1**, 58–71 (2019).

13. Broido, A. D. & Clauset, A. Scale-free networks are rare. *Nat Commun* **10**, 1017 (2019).

14. Bassett, D. S., Khambhati, A. N. & Grafton, S. T. Emerging Frontiers of Neuroengineering: A Network Science of Brain Connectivity. *Annu. Rev. Biomed. Eng.* **19**, 327–352 (2017).

15. Barabási, A.-L. & Albert, R. Emergence of Scaling in Random Networks. *Science* **286**, 509–512 (1999).

16. van den Heuvel, M. P. & Sporns, O. Network hubs in the human brain. *Trends in Cognitive Sciences* **17**, 683–696 (2013).

17. Bonifazi, P. *et al.* GABAergic Hub Neurons Orchestrate Synchrony in Developing Hippocampal Networks. *Science* **326**, 1419–1424 (2009).

18. Picardo, M. A. *et al.* Pioneer GABA Cells Comprise a Subpopulation of Hub Neurons in the Developing Hippocampus. *Neuron* **71**, 695–709 (2011).

19. Bocchio, M. *et al.* Hippocampal hub neurons maintain distinct connectivity throughout their lifetime. *Nat Commun* **11**, 4559 (2020).

20. Elam, J. S. *et al.* The Human Connectome Project: A retrospective. *NeuroImage* **244**, 118543 (2021).

21. Stiles, J. & Jernigan, T. L. The Basics of Brain Development. *Neuropsychol Rev* **20**, 327–348 (2010).

22. Altman, J. & Bayer, S. A. Development of the brain stem in the rat. I. Thymidine-radiographic study of the time of origin of neurons of the lower medulla. *J. Comp. Neurol.* **194**, 1–35 (1980).

23. Altman, J. & Bayer, S. A. Development of the brain stem in the rat. III. Thymidine-radiographic study of the time of origin of neurons of the vestibular and auditory nuclei of the upper medulla. *J. Comp. Neurol.* **194**, 877–904 (1980).

24. Altman, J. & Bayer, S. A. Development of the brain stem in the rat. V. Thymidine-radiographic study of the time of origin of neurons in the midbrain tegmentum. *J. Comp. Neurol.* **198**, 677–716 (1981).

25. Steindler, D. A. & Trosko, B. K. Two types of locus coeruleus neurons born on different embryonic days in the mouse. *Anat Embryol* **179**, 423–434 (1989).

26. Altman, J. & Bayer, S. A. Development of the brain Stem in the rat. II. Thymidine-radiographic study of the time of origin of neurons of the upper medulla, excluding the vestibular and auditory nuclei. *J. Comp. Neurol.* **194**, 37–56 (1980).

27. Kebschull, J. M. *et al.* High-Throughput Mapping of Single-Neuron Projections by Sequencing of Barcoded RNA. *Neuron* **91**, 975–987 (2016).

28. Goto, T. *et al.* Neurodegeneration of Trigeminal Mesencephalic Neurons by the Tooth Loss Triggers the Progression of Alzheimer's Disease in 3×Tg-AD Model Mice. *JAD* **76**, 1443–1459 (2020).

29. Beardmore, R., Hou, R., Darekar, A., Holmes, C. & Boche, D. The Locus Coeruleus in Aging and Alzheimer's Disease: A Postmortem and Brain Imaging Review. *JAD* **83**, 5–22 (2021).

30. Jacobs, H. I. L. *et al.* In vivo and neuropathology data support locus coeruleus integrity as indicator of Alzheimer's disease pathology and cognitive decline. *Sci. Transl. Med.* **13**, eabj2511 (2021).

31. Cossart, R. Operational hub cells: a morpho-physiologically diverse class of GABAergic neurons united by a common function. *Current Opinion in Neurobiology* **26**, 51–56 (2014).

32. Mòdol, L. *et al.* Spatial Embryonic Origin Delineates GABAergic Hub Neurons Driving Network Dynamics in the Developing Entorhinal Cortex. *Cerebral Cortex* **27**, 4649–4661 (2017).

33. Molnár, Z. *et al.* New insights into the development of the human cerebral cortex. *J. Anat.* **235**, 432–451 (2019).

34. Gal, E. *et al.* The Role of Hub Neurons in Modulating Cortical Dynamics. *Front. Neural Circuits* **15**, 718270 (2021).

35. Krook-Magnuson, E., Szabo, G. G., Armstrong, C., Oijala, M. & Soltesz, I. Cerebellar Directed Optogenetic Intervention Inhibits Spontaneous Hippocampal Seizures in a Mouse Model of Temporal Lobe Epilepsy. *eneuro* **1**, ENEURO.0005-14.2014 (2014).

36. Dehorter, N. & Del Pino, I. Shifting Developmental Trajectories During Critical Periods of Brain Formation. *Front. Cell. Neurosci.* **14**, 283 (2020).

37. Wong-Riley, M. T. T. The critical period: neurochemical and synaptic mechanisms shared by the visual cortex and the brain stem respiratory system. *Proc. R. Soc. B.* **288**, 20211025 (2021).

38. Varier, S. & Kaiser, M. Neural Development Features: Spatio-Temporal Development of the Caenorhabditis elegans Neuronal Network. *PLoS Comput Biol* **7**, e1001044 (2011).

39. Pavlovic, D. M., Vértes, P. E., Bullmore, E. T., Schafer, W. R. & Nichols, T. E. Stochastic Blockmodeling of the Modules and Core of the Caenorhabditis elegans Connectome. *PLoS ONE* **9**, e97584 (2014).

40. Bassett, D. S. *et al.* Efficient Physical Embedding of Topologically Complex Information Processing Networks in Brains and Computer Circuits. *PLoS Comput Biol* **6**, e1000748 (2010).

41. Nieuwenhuys, R. *et al. The Central Nervous System of Vertebrates*. (Springer Berlin / Heidelberg, 1997).

42. Suárez, L. E. *et al. A connectomics-based taxonomy of mammals*. http://biorxiv.org/lookup/doi/10.1101/2022.03.11.483995 (2022) doi:10.1101/2022.03.11.483995.

43. Rueda-Alaña, E. & García-Moreno, F. Time in Neurogenesis: Conservation of the Developmental Formation of the Cerebellar Circuitry. *Brain Behav Evol* 1–15 (2021) doi:10.1159/000519068.

44. Arnatkeviciute, A., Fulcher, B. D., Bellgrove, M. A. & Fornito, A. Where the genome meets the connectome: Understanding how genes shape human brain connectivity. *NeuroImage* **244**, 118570 (2021).

45. Stefanis, L. -Synuclein in Parkinson's Disease. *Cold Spring Harbor Perspectives in Medicine* **2**, a009399–a009399 (2012).

46. Zarranz, J. J. *et al.* The new mutation, E46K, of α-synuclein causes parkinson and Lewy body dementia: New α-Synuclein Gene Mutation. *Ann Neurol.* **55**, 164–173 (2004).

47. Paul, K. C. *et al.* APOE, MAPT, and COMT and Parkinson's Disease Susceptibility and Cognitive Symptom Progression. *JPD* **6**, 349–359 (2016).

48. Verghese, P. B., Castellano, J. M. & Holtzman, D. M. Apolipoprotein E in Alzheimer's disease and other neurological disorders. *The Lancet Neurology* **10**, 241–252 (2011).

49. Ulland, T. K. & Colonna, M. TREM2 — a key player in microglial biology and Alzheimer disease. *Nat Rev Neurol* **14**, 667–675 (2018).

50. Diaz-Lucena, D. *et al.* TREM2 expression in the brain and biological fluids in prion diseases. *Acta Neuropathol* **141**, 841–859 (2021).

51. Cuccaro, M. L. *et al. SORL1* mutations in early- and late-onset Alzheimer disease. *Neurol Genet* **2**, e116 (2016).

52. Narita, A. *et al.* Clustering by phenotype and genome-wide association study in autism. *Transl Psychiatry* **10**, 290 (2020).

53. Stessman, H. A. F. *et al.* Targeted sequencing identifies 91 neurodevelopmental-disorder risk genes with autism and developmental-disability biases. *Nat Genet* **49**, 515–526 (2017).

54. Claes, L. *et al.* De Novo Mutations in the Sodium-Channel Gene SCN1A Cause Severe Myoclonic Epilepsy of Infancy. *The American Journal of Human Genetics* **68**, 1327–1332 (2001).

55. Bassett, D. S. & Bullmore, E. T. Human brain networks in health and disease. *Current Opinion in Neurology* **22**, 340–347 (2009).

56. Rolls, E. T., Huang, C.-C., Lin, C.-P., Feng, J. & Joliot, M. Automated anatomical labelling atlas 3. *NeuroImage* **206**, 116189 (2020).

57. Nowinski, W. L. Evolution of Human Brain Atlases in Terms of Content, Applications, Functionality, and Availability. *Neuroinform* **19**, 1–22 (2021).

58. Nieuwenhuys, R. & Puelles, L. *Towards a New Neuromorphology*. (Springer International Publishing, 2016). doi:10.1007/978-3-319-25693-1.

59. Nieuwenhuys, R. & Nieuwenhuys, R. Principles of Current Vertebrate Neuromorphology. *Brain Behav Evol* **90**, 117–130 (2017).

60. Glasser, M. F. *et al.* The minimal preprocessing pipelines for the Human Connectome Project. *NeuroImage* **80**, 105–124 (2013).

61. Desikan, R. S. *et al.* An automated labeling system for subdividing the human cerebral cortex on MRI scans into gyral based regions of interest. *NeuroImage* **31**, 968–980 (2006).

62. Pauli, W. M., Nili, A. N. & Tyszka, J. M. A high-resolution probabilistic in vivo atlas of human subcortical brain nuclei. *Sci Data* **5**, 180063 (2018).

63. Edlow, B. L. *et al.* Neuroanatomic Connectivity of the Human Ascending Arousal System Critical to Consciousness and Its Disorders. *J Neuropathol Exp Neurol* **71**, 531–546 (2012).

64. Diez, I. *et al.* A novel brain partition highlights the modular skeleton shared by structure and function. *Sci Rep* **5**, 10532 (2015).

65. Bonifazi, P. *et al.* Structure–function multi-scale connectomics reveals a major role of the fronto-striato-thalamic circuit in brain aging. *Hum Brain Mapp* **39**, 4663–4677 (2018).

66. Zhang, Y., Brady, M. & Smith, S. Segmentation of brain MR images through a hidden Markov random field model and the expectation-maximization algorithm. *IEEE Trans. Med. Imaging* **20**, 45–57 (2001).

67. Hawrylycz, M. J. *et al.* An anatomically comprehensive atlas of the adult human brain transcriptome. *Nature* **489**, 391–399 (2012).

68. Shen, E. H., Overly, C. C. & Jones, A. R. The Allen Human Brain Atlas. *Trends in Neurosciences* **35**, 711–714 (2012).

69. Arnatkevičiūtė, A., Fulcher, B. D. & Fornito, A. A practical guide to linking brain-wide gene expression and neuroimaging data. *NeuroImage* **189**, 353–367 (2019).

70. Diez, I. & Sepulcre, J. Unveiling the neuroimaging-genetic intersections in the human brain. *Current Opinion in Neurology* **Publish Ahead of Print**, (2021).

71. Zhou, Y. *et al.* Metascape provides a biologist-oriented resource for the analysis of systems-level datasets. *Nat Commun* **10**, 1523 (2019).

72. Shannon, P. *et al.* Cytoscape: A Software Environment for Integrated Models of Biomolecular Interaction Networks. *Genome Res.* **13**, 2498–2504 (2003).

Legends

Figure 1. From circuits' embryogenic age to brain networks and transcriptomics. *(A) Sagittal schemes of the early embryonic human brain; left scheme represents the neuromeres and fundamental regions of development; right scheme displays the location of the 18 MACs within the early embryonic human brain colour-coded according to their FirsT. (B) Scheme of the neuroimage analysis pipeline. Brain networks were reconstructed from healthy adult subjects scanned with MRI at 7T within the HCP initiative. For each subject, the structural and functional networks were reconstructed using respectively probabilistic tractography and resting-state activity. For every pair of ROIs (total 2566 ROIs), the structural connectivity matrix represents the putative number of fibers connecting them, while the functional connectivity matrix reports the correlation in their activity as revealed by the BOLD time series. The average across subjects were used as final representative brain networks (see Methods). From the 2566 ROIs' matrices, the 18 MACs' networks were reconstructed and represents for each pair of MACs the average links between the ROIs forming them (see Methods). To identify patterns between networks' topology and neurogenesis, the correlation between the nodes' metrics (centrality or segregation) and embryonic age was calculated. (C) Brain transcriptome data from AHBA dataset (see methods) was used to search for protein coding genes with a high similarity between its spatial brain expression and embryonic age. Functional annotations of the obtained genes were further computed using overrepresentation analysis to find significantly associated biological processes and cellular components associated with embryonic age.*

Figure 2. Scatter plots of nodes' centrality/segregation, links' probability/weight, vs. FirsT, in the high and low resolution structural-functional networks. *(A) Scatter plots of the nodes' centrality (each row corresponds to a different metric specified on the left) and segregation (bottom row) as a function of the embryonic age. Red and blue colours mark respectively the structural and functional cases. First and second columns from left represent as violine plots the results for the 2566 ROIs case where the mean of each group (i.e. ROIs within a MAC) is plotted in black, while the third and fourth columns represents the 18 MACs' case. (B) Scatter plots of the link weights (left y-axis) as function of difference of first neurogenic birthdate. Colours and columns represent the same cases*

as in panel A. In the 2566 ROIs case, the violine plots show the link weight distributions while the solid blue/red lines plot the average values. Black solid lines show the exponential (linear) fit on the average values for the structural (functional) case. The link probability is represented by the right y-axes and displayed as dots, and the broken black line show the exponential (linear) fit for the structural (functional) case.

Figure 3. Visualization of brain connectivity and first neurogenic birthdate. *(A) The glass brain maps of the eighteen MACs represents in colour codes the FirsT (A1; see colour-bar on the left) and the z-score (see colour-bar on the right) of the eigenvector centrality for the* SC^{LR} *(A2) and the* FC^{LR} *(A3). (B) Linear temporal representation with arches of the MACs structural connectivity for the earliest (B1) generated MAC (Locus Coeruleus, FirsT 28), for a representative mid-term (B2) generated MAC (Hippocampus, FirsT 40) and the latest (B3) generated MAC (Occipital Cortex, FirsT 54). The x-axis represents the developmental time along the several FirsT, where the different MACs are located according to their FirsT. Note that Basal Ganglia and Cerebellum are overlapped since their first neurogenesis coincides at day 36. The thickness of top black arches is proportional to the link weight between the MACs as extracted from the 18-nodes adjacency matrix. Broken black lines mark the presence of connections but with very small weight (i.e. below the lowest threshold for visualization of solid lines).*

Figure 4. Transcriptomic of brain circuits according to embryogenic age. *(A) Mean spatial similarity between 20,737 protein-coding genes with 18 circuits time of birth, structural connectivity centrality projected to 90 regions and functional connectivity centrality projected to 90 regions was computed. (B) 787 genes from the positive tail were used to compute overrepresentation analysis for biological processes and cellular component annotations. (C) A network analysis of biological process and cellular component terms was computed. Different colours represent different annotation clusters and the edges the kappa score representing number of common genes in the functional annotations. Scatterplots displaying the mean gene expression of the genes related to brain development with time of birth and functional and structural connectivity centrality are displayed.*

Figure 5. Correlations between genes' transcriptomic and hubness in relation to autism, epilepsy, Parkinson's and Alzheimer's. *For each gene the spatial expression in the brain has been correlated to the spatial map of the eigenvector centrality (note that given the subsampled brain transcriptomics, ninety brain regions were considered, see Methods).* ***A*** *Probability distribution of correlations (blue histogram, left axis) between transcriptomics (20787 genes) and structural (A1) - functional (A2) eigenvector centrality. The relevance score of the genes listed for each disease (according to GeneCars.org, see Methods) has been plotted with black dots (right axis). Red dots mark the relevance scores for gene reported for each given disease in the GWAS dataset (see Methods). Vertical broken lines highlight the +/-1.64 standard deviation range. Green labels and arrows mark representative GWAS genes with top relevance scores beyond the highlighted 1.64 standard deviation range.* ***B*** *For each disease, the count of related genes listed by the GWAS in 5 percentiles intervals of the correlation distribution (blue*

histogram of panel A) is plotted (red line and dots). The threshold for p<0.01 is plotted as a broken horizontal black line. Black arrows mark the extremities of the correlation distributions with significant higher number of GWAS-genes, and related p-value. B1 and B2 refers respectively to structural and functional eigenvector centrality. Note that legends are gray-shaded.

Table 1 Developmental information of the human brain macro-circuits under research. *The table includes the list of 18 MACs, the developmental brain region from which each MAC derives, the main anatomical structures each MAC comprises within the brain, information about the earliest stage at which neurogenesis (FirsT) is observed or predicted in the human brain and other mammalian species, and the number of ROIs obtained in each MAC.*

Table 2: correlation between nodes' centrality/segregation, and FirsT for the SCNs and FCNs. *The partial Spearman correlation regressing out the white matter ratio per ROI/MAC is reported with its associate p-value. Not significant (p>0.05) or low correlations (|SP-pCorr|<0.15) are marked with an asterisk.*

References Table 1

Achim, K., Peltopuro, P., Lahti, L., Li, J., Salminen, M., Partanen, J., 2012. Distinct developmental origins and regulatory mechanisms for GABAergic neurons associated with dopaminergic nuclei in the ventral mesodiencephalic region. Dev. 139, 2360–2370. https://doi.org/10.1242/dev.076380

Altman, J., Bayer, S.A., 1980a. Development of the brain stem in the rat. 1. Thymidine-Radiographic Study of the Time of Origin of Neurons of the Lower Medulla. J. Comp. Neurol. 194, 1–35. 10.1002/cne.901940102

Altman, J., Bayer, S.A., 1980b. Development of the brain stem in the rat. III. Thymidine-radiographic study of the time of orgin of neurons of the vestibular and auditory nuclei of tghe upper medulla. J. Comp. Neurol. 194, 877–904. 10.1002/cne.901940410

Altman, J., Bayer, S.A., 1980c. Development of the brain stem in the rat. V. Thymidine-Radiographic Study of the Time of Origin of Neurons in the Midbrain Tegmentum. J. Comp. Neurol. 198, 677–716. https:// 10.1002/cne.901980409

Altman, J., Bayer, S.A., 1979. Development of the Diencephalon in the Rat. IV Quantitative study of the time of origin of neurons and the internuclear chronological gradients in the thalamus. J. Comp. Neurol. 188, 455–472. https://doi.org/10.1002/cne.901940411

Altman, J., Bayer, S.A., 1978a. Development of the Diencephalon in the rat. I. Autoradiographic study of the time of origin and settling patterns of neurons of the hypothalamus. J. Comp. Neurol. 182, 945–971. https://doi.org/10.1002/cne.901820511

Altman, J., Bayer, S.A., 1978b. Development of the Diencephalon in the Rat II: Correlation of the embryonic development of the hypothalamus with the time of origin of its neurons. J. Comp. Neurol. 182, 973:994.

Altman, J., Bayer, S.A., 1978c. Development of the Diencephalon in the Rat. III Ontogeny of the specialized ventricular linings of the hypothalamic third ventricle. J. Comp. Neurol. 182, 995–1016.

Bayer, A., 1980. Development of the Hippocampal Region in the Rat. I - Neurogenesis Examined With 3H-Thymidine Autoradiography. J. Comp. Neurol. 190, 87–114.

Bayer, S.A., 1986. Neurogenesis in the rat primary olfactory cortex. Int. J. Dev. Neurosci. 4, 251–271.

Bayer, S.A., Wills, K. V., Triarhou, L.C., Ghetti, B., 1995. Time of neuron origin and gradients of neurogenesis in midbrain dopaminergic neurons in the mouse. Exp. Brain Res. 105, 191–199. https://doi.org/10.1007/BF00240955

Brand, S., Rakic, P., 1980. Neurogenesis of the nucleus accumbens septi and neighboring septal nuclei in the rhesus monkey: a combined [3H] thymidine and electron microscopic study. Neuroscience 5, 2125–2138.

Charvet, C.J., 2014. Distinct developmental growth patterns account for the disproportionate expansion of the rostral and caudal isocortex in evolution. Front. Hum. Neurosci. 8, 1–11. https://doi.org/10.3389/fnhum.2014.00190

Eerdenburg, F.J.C.M. Van, Rakic, P., 1994. Early neurogenesis in the anterior hypothalamus of the rhesus monkey. Dev. Brain Res. 79, 290–296.

Granger, B., Tekaia, F., Le Sourd, A.M., Rakic, P., Bourgeois, J. -P, 1995. Tempo of neurogenesis and synaptogenesis in the primate cingulate mesocortex: Comparison with the neocortex. J. Comp. Neurol. 360, 363–376. https://doi.org/10.1002/cne.903600212

Leto, K., Carletti, B., Williams, I.M., Magrassi, L., Rossi, F., 2006. Different Types of Cerebellar GABAergic Interneurons Originate from a Common Pool of Multipotent Progenitor Cells. J. Neurosci. 26, 11682–11694. https://doi.org/10.1523/JNEUROSCI.3656-06.2006

Mcconnell, J., Angevine, J.A.Y.B., 1983. Time of neuron origin in the amygdaloid complex of the mouse. Brain Res. 272, 150–156.

Miale, I.L., Sidman, R.L., 1961. An autoradiographic analysis of histogenesis in the mouse cerebellum. Exp. Neurol. 4, 277–296. https://doi.org/10.1016/0014-4886(61)90055-3

Rakic, P., 2002. Pre- and post-developmental neurogenesis in primates. Clin. Neurosci. Res. 2 2, 29–39.

Reillo, I., Borrell, V., 2011. Germinal Zones in the Developing Cerebral Cortex of Ferret : Ontogeny , Cell Cycle Kinetics , and Diversity of Progenitors Germinal Zones in the Developing Cerebral Cortex of Ferret : Ontogeny , Cell Cycle Kinetics , and Diversity of Progenitors. Cereb. Cortex. https://doi.org/10.1093/cercor/bhr284

Soma, M., Aizawa, H., Ito, Y., Maekawa, M., Osumi, N., Nakahira, E., Okamoto, H., Tanaka, K., Yuasa, S., 2009. Development of the mouse amygdala as revealed by

enhanced green fluorescent protein gene transfer by means of in utero electroporation. J. Comp. Neurol. 513, 113–128. https://doi.org/10.1002/cne.21945

Steindler, D.A., Trosko, B.K., 1989. Two types of locus coeruleus neurons born on different embryonic days in the mouse. Anat. Embryol. (Berl). 179, 423–434.

Workman, A.D., Charvet, C.J., Clancy, B., Darlington, R.B., Finlay, B.L., 2013. Modeling Transformations of Neurodevelopmental Sequences across Mammalian Species. J. Neurosci. 33, 7368–7383. https://doi.org/10.1523/JNEUROSCI.5746-12.2013

Table 1

	Major developmental brain area	Circuit	fMRI Comprised structures	Earliest stage in human (translated)	Earliest stage in other species	Source	Observations	ROIs #
1	Rhombencephalon	**Locus Coeruleus**	Locus Coeruleus	**28**	Rat - Soon before E12; Mouse - E9	Altman and Bayer, 1980a,b,c; Steindler and Trosko, 1989	Likely one of the earliest generated nucleus. Noradrenergic neuronsare the earliest-born within the LC	2
2	Rhombencephalon	**Medulla Oblongata**	Pons and Medulla oblongata	**31**	Rat - Soon after 12	Altman and Bayer, 1980a	Brainstem neurogenesis starts much earlier than in the rest of the brain. However we could not segment its many different compartments by fMRI and so it appears fused in one single circuit.	40
3	Mesencephalon	**Midbrain**	Superior colliculus, inferior colliculus, tegmental midbrain	**32**	Mouse - E10.5	Bayer et al., 1995; Achim et al., 2012	Substantia nigra pars reticulata is the earliest mesencephalic nucleus to start neurogenesis	23
4	Seconary Prosencephalon	**Hypothalamus**	Hypothalamus, mammilary bodies	**34**	Rat - E12; Macaque - E33; Cat - E21	Altman and Bayer, 1978a,b; Eerdenburg and Rakic, 1994; translatingtime.org	Lateral hypothalamic nuclei (lateral hypothalamic nucleus, lateral preoptic area and lateral mammilary bodies) start hypothalamic neurogenesis at	18
	Telencephalon	**Olfactory**	Olfactory Cortices	**34**	Mouse E11	translatingtime.org (Workman et al., 2013)	Unique segmentation and ROI identification with Hypothalamus	
5	Rhombencephalon	**Raphe Nuclei**	Raphe nuclei	**35**	Rat E12		Neurogenesis in the Raphe nuclei starts in the Raphe Magnus nucleus	3
6	Telencephalon	**Basal Ganglia**	Caudate, Putamen, Accumbens, Septum	**36**	Mouse - E11; Macaque - E38	Brand and Rakic, 1980	Accumbens starts neurogenesis at E38 in macaque; Striatum and globus pallidus start soon after.	77
7	Rhombencephalon	**Cerebellum**	Cerebellar cortex, deep cerebellar nuclei	**36**	Mouse E11; Rat - E13	Miale and Sidman, 1961; Altman and Bayer, 1978c; Leto et al., 2006	Earliest neurons are projection neruons of the deep cerebellar nuclei, followed by Purkinje neurons.	275
8	Telencephalon	**Entorhinal**	Entorhinal cortex	**37**	Rat - soon after E14	Bayer, 1980a	Neurogenesis starts earlier to other parahippocampal cortices	11
9	Telencephalon	**Amygdala**	Pallial amygdala, subpallial amygdala	**38**	Mouse E11	McConnell and Angevine, 1983; Soma et al., 2009	Neurogenesis starts with GABAergic populations of central and medial nuclei, followed by the glutamatergic neurons of the baso-lateral complex	8
10	Telencephalon	**Hippocampus**	Amon horn, Dentate gyrus	**40**	Rat E14.5	Bayer, 1980a	Earliest neurons occupy the superficial and deep layers of the Ammon´s horn (CA1 to CA3), and the hilus	21
11	Telencephalon	**Posterior cingulum**	Posterior cingular cortex	**42**	Rat E14.5	translatingtime.org	Inferred from translatingtime.org Earlier than the anterior cingulate cortex	22
12	Telencephalon	**Parahippocampal cortices**	Parahippocampal cortex	**44**	Rat E15	Bayer, 1980a	Includes subiculum and parasubiculum. Unique segmentation and ROI identification with Insula	107
	Telencephalon	**Insula**	Insular cortex	**44**	Rat E15	Bayer, 1986	First insular neurons occupy the dep layers of the ventral agranular insular cortex.	
13	Telencephalon	**Anterior Cingulate cortex**	Caudal Anterior Cingulate, Rostral Anterior Cingulate	**45**	Macaque - E40	Granger et al., 1995	First Layer VI neurons in the anterior cingulate cortex were revelaed with [3H]-thymidine injection at E40 in the macaque brain	37
14	Diencephalon	**Thalamus**	Thalamic nuclei: LP, VL, VPL, LGN, MGN, Pulvinar,	**46**	Rat - E14	Altman and Bayer, 1979	Several thalamic nuclei (VB, VE, LGN, PO, MGN and LP) start neurogenesis at E14 in the rat brain.	28
15	Telencephalon	**Frontal cortex**	Caudal middle frontal, lateral orbito frontal, medial orbito frontal, paracentral, pars opercularis, pars orbitalis, pars triangularis, precentral, rostral middle frontal, frontal pole and superior frontal cortices	**48**	Macaque - E40; Ferret - E30; Mouse - E11.5	Rakic, 2002; Reillo and Borrell, 2011; Charvet, 2014; translatingtime.org	Neurogenesis in the cortex starts synchronously throughout all cortical areas. The earliest-generated cortical populations are the Cajal-Retzius cells of the marginal zone and the subplate neurons of layer 6b. Most of these neurons die early after birth, which is why we considered the early generation of deep cortical layers as the onset of a functional cortical neurogenesis. In this layers, there is a gradient of neurogenesis starting first at the rostral pole of the cortex, and finishing last at the caudal regions. In macaque, frontal cortex starts at E45, and occipital cortex starts at E54. In human, we estimate ths gradient as a 2-day difference between cortical lobes.	719
16	Telencephalon	**Parietal cortex**	Inferior parietal, postcentral, precuneus, superior parietal and supramarginal cortices	**50**				502
17	Telencephalon	**Temporal cortex**	Banks of the Superior Temporal Sulcus, fusiform, inferior temporal, superior temporal, and transverse temporal cortices	**52**				384
18	Telencephalon	**Occipital cortex**	Cuneus, Lateraloccipital cortex, lingual cortex, pericalcarine cortex	**54**				289

Table 2

METRICS	ROIs - 2566 nodes				MACs – 18 nodes			
	hr-SCN		hr-FCN		lr-SCN		lr-FCN	
	SP-pCorr	*p-val*	*SP-pCorr*	*p-val*	*SP-pCorr*	*p-val*	*SP-pCorr*	*p-val*
Strength (NS)	-0,25	0	0,23	0	-0,77	0,0003	-0,47	0,06*
Eigenvector (EC)	-0,44	0	0,26	0	-0,81	0,00007	-0,51	0,035
Pagerank (PC)	-0,17	0	0,20	0	-0,59	0,01	-0,46	0,06*
Subgraph (SC)	-0,29	0	0,26	0	-0,74	0,0007	-0,54	0,02
Betweenness (BC)	-0,077*	0,00008	0,12	3 10-09	-0,58	0,015	-0,057	0,83*
1st-neighbour (AFNS)	-0,27	0	0,28	0	-0,7	0,002	-0,83	4 10-05
Clustering (CC)	0,002	0,9*	0,33	0	-0,77	0,0003	-0,37	0,14*

Figure 1

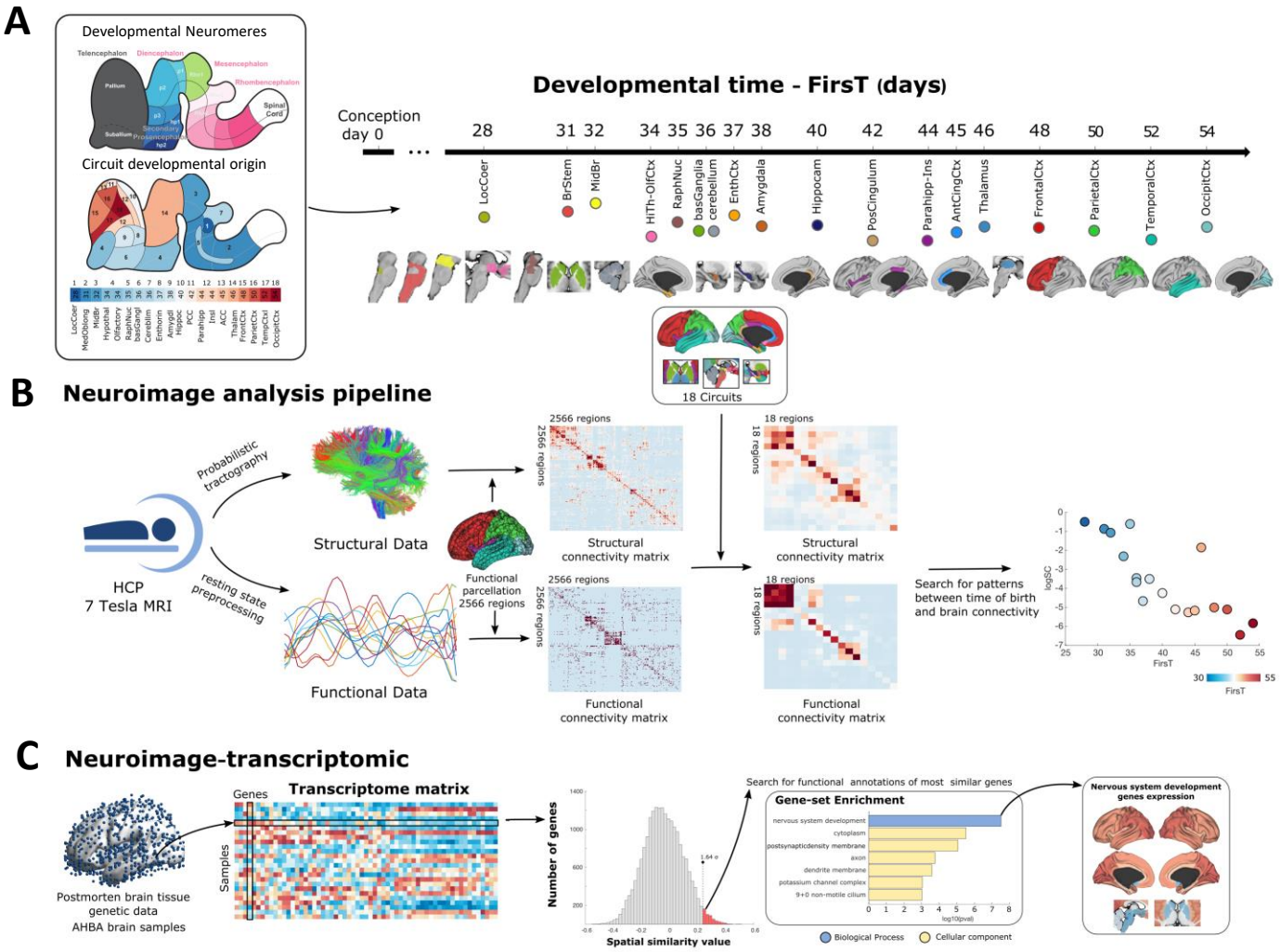
A
Developmental Neuromeres
Telencephalon
Diencephalon
Mesencephalon
Rhombencephalon
Pallium
Subpallium
Spinal Cord
Circuit developmental origin
Developmental time - FirstT (days)
Conception day 0
28
31 32
34 35 36 37 38
40
42
44 45 46
48
50
52
54
LocCoer
BrStem
MidBr
HiTh-OlfCtx
RaphNuc
basGanglia
cerebellum
EnthCtx
Amygdala
Hippocam
PosCingulum
Parahipp-Ins
AntCingCtx
Thalamus
FrontalCtx
ParietalCtx
TemporalCtx
OccipitCtx
18 Circuits
B
Neuroimage analysis pipeline
Probabilistic tractography
resting state preprocessing
HCP
7 Tesla MRI
Structural Data
Functional Data
Functional parcellation
2566 regions
2566 regions
Structural connectivity matrix
Functional connectivity matrix
18 regions
Structural connectivity matrix
Functional connectivity matrix
Search for patterns between time of birth and brain connectivity
logSC
FirstT
C
Neuroimage-transcriptomic
Postmorten brain tissue genetic data
AHBA brain samples
Genes
Transcriptome matrix
Samples
Number of genes
Spatial similarity value
Search for functional annotations of most similar genes
Gene-set Enrichment
nervous system development
cytoplasm
postsynapticdensity membrane
axon
dendrite membrane
potassium channel complex
9+0 non-motile cilium
log10(pval)
Biological Process
Cellular component
Nervous system development genes expression

Figure 2

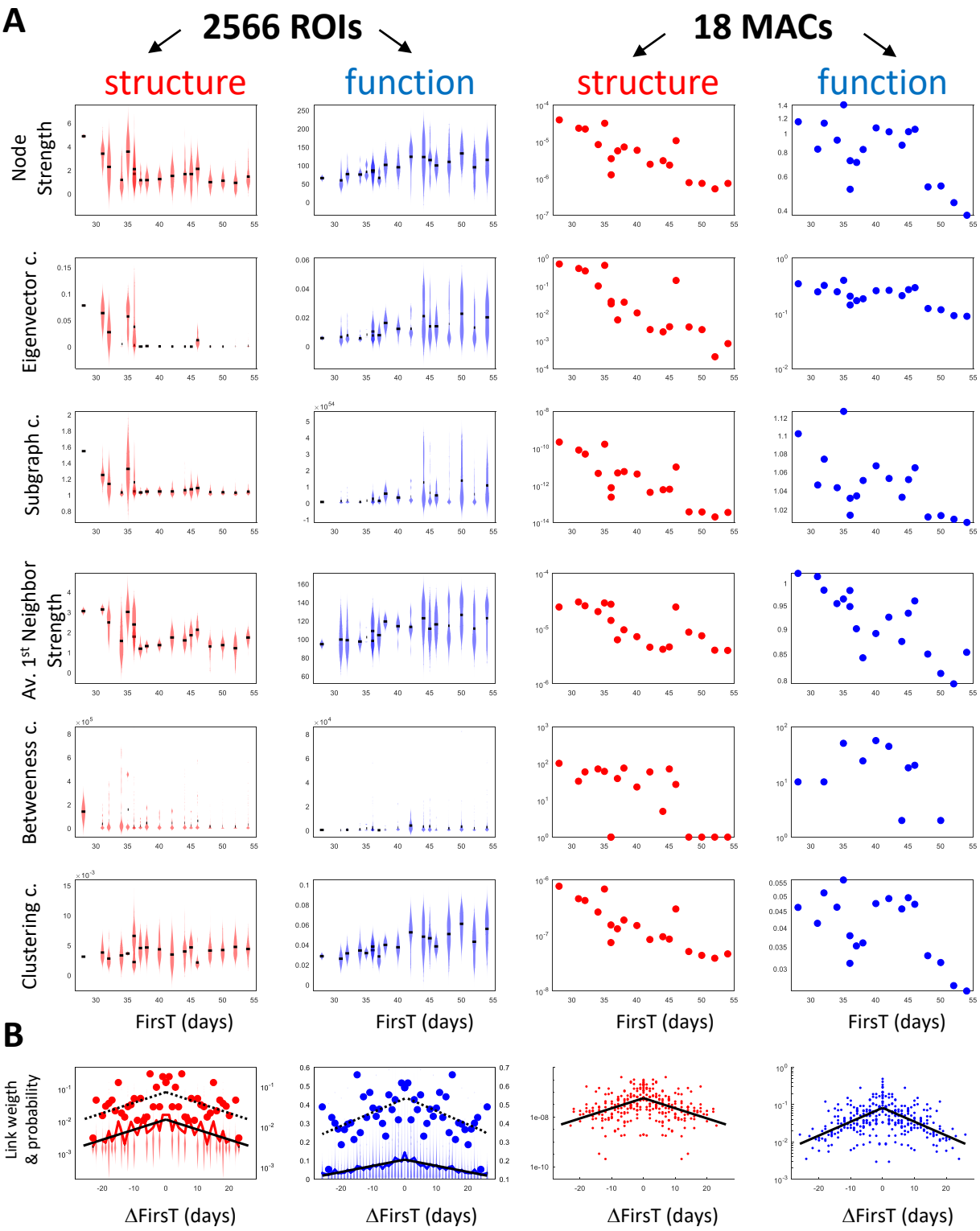
A
2566 ROIs
18 MACs
structure
function
structure
function
Node Strength
Eigenvector c.
Subgraph c.
Av. 1st Neighbor Strength
Betweeness c.
Clustering c.
FirsT (days)
B
Link weigth & probability
ΔFirsT (days)

Figure 3

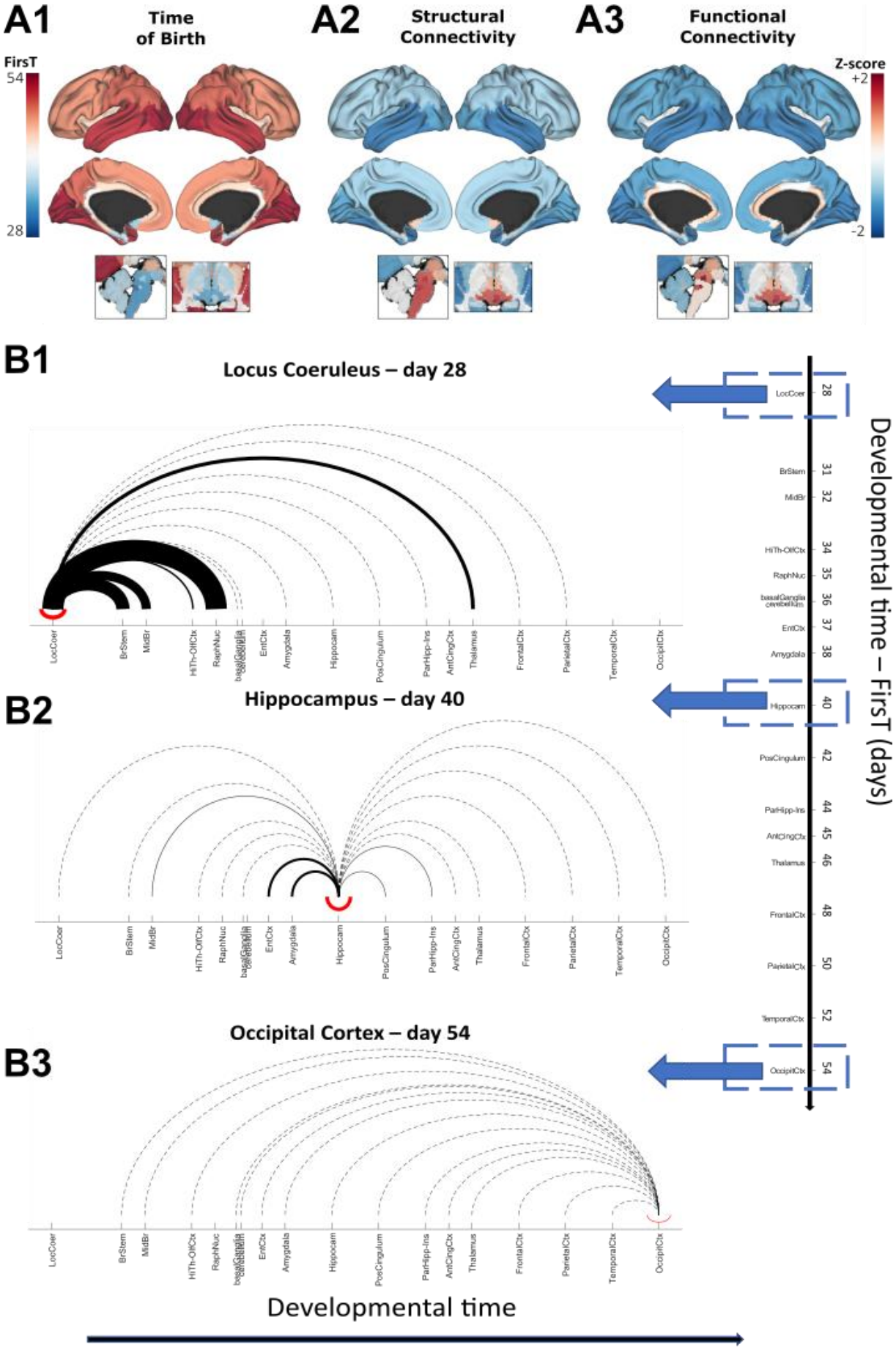
A1
Time of Birth
FirsT
54
28
A2
Structural Connectivity
A3
Functional Connectivity
Z-score
+2
-2
B1
Locus Coeruleus – day 28
B2
Hippocampus – day 40
B3
Occipital Cortex – day 54
LocCoer
BrStem
MidBr
HiTh-OlfCtx
RaphNuc
basalGanglia
cerebellum
EntCtx
Amygdala
Hippocam
PosCingulum
ParHipp-Ins
AntCingCtx
Thalamus
FrontalCtx
ParietalCtx
TemporalCtx
OccipitCtx
Developmental time – FirsT (days)
Developmental time

Figure 4

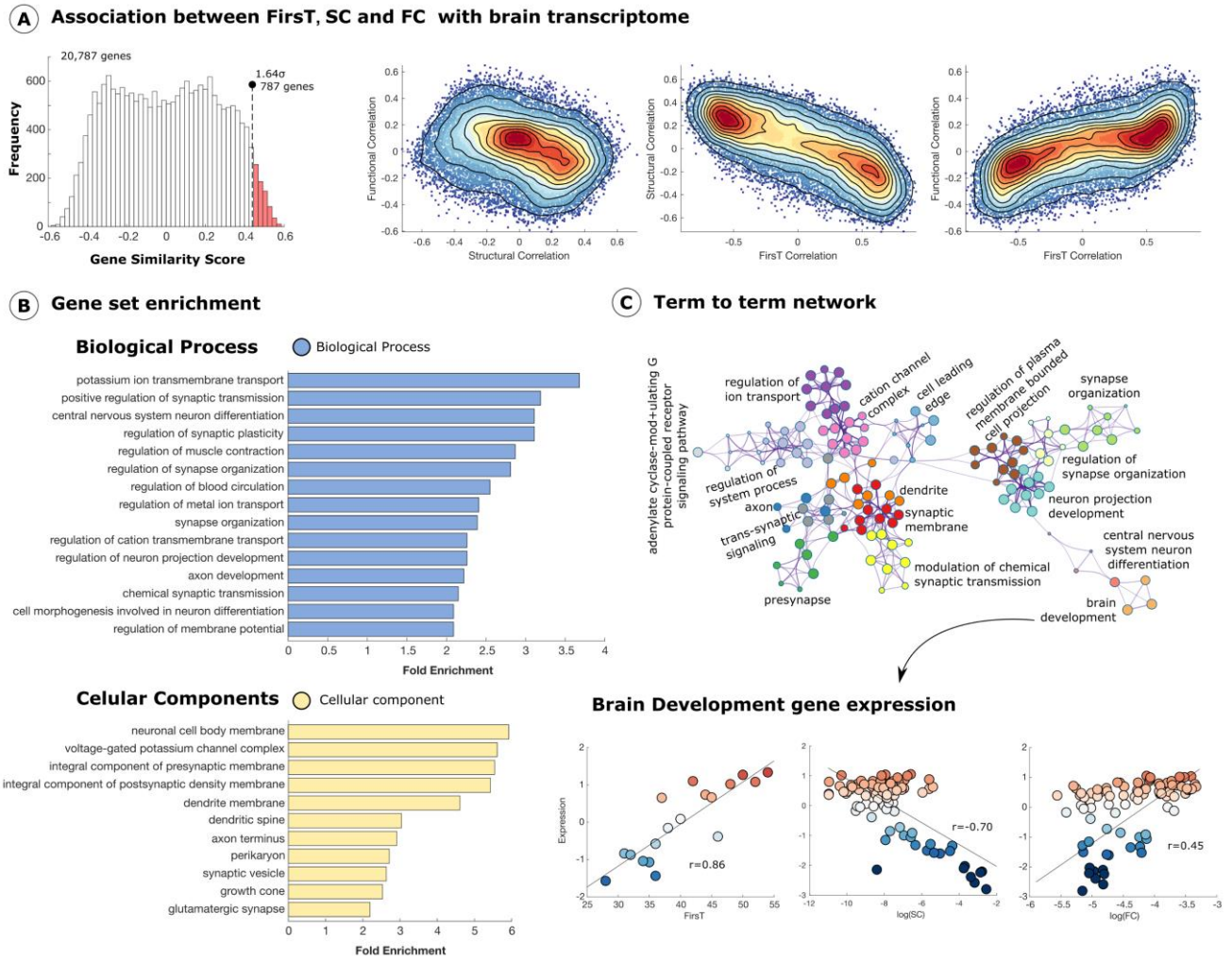
A
Association between FirsT, SC and FC with brain transcriptome
20,787 genes
1.64σ
787 genes
Frequency
Gene Similarity Score
Functional Correlation
Structural Correlation
Structural Correlation
FirsT Correlation
Functional Correlation
FirsT Correlation
B
Gene set enrichment
Biological Process
Biological Process
potassium ion transmembrane transport
positive regulation of synaptic transmission
central nervous system neuron differentiation
regulation of synaptic plasticity
regulation of muscle contraction
regulation of synapse organization
regulation of blood circulation
regulation of metal ion transport
synapse organization
regulation of cation transmembrane transport
regulation of neuron projection development
axon development
chemical synaptic transmission
cell morphogenesis involved in neuron differentiation
regulation of membrane potential
Fold Enrichment
Celular Components
Cellular component
neuronal cell body membrane
voltage-gated potassium channel complex
integral component of presynaptic membrane
integral component of postsynaptic density membrane
dendrite membrane
dendritic spine
axon terminus
perikaryon
synaptic vesicle
growth cone
glutamatergic synapse
Fold Enrichment
C
Term to term network
adenylate cyclase-mod+ulating G protein-coupled receptor signaling pathway
regulation of ion transport
cation channel complex
cell leading edge
regulation of plasma membrane bounded cell projection
synapse organization
regulation of synapse organization
regulation of system process
axon
dendrite
synaptic membrane
trans-synaptic signaling
neuron projection development
central nervous system neuron differentiation
modulation of chemical synaptic transmission
presynapse
brain development
Brain Development gene expression
Expression
FirsT
r=0.86
log(SC)
r=-0.70
log(FC)
r=0.45

Figure 5

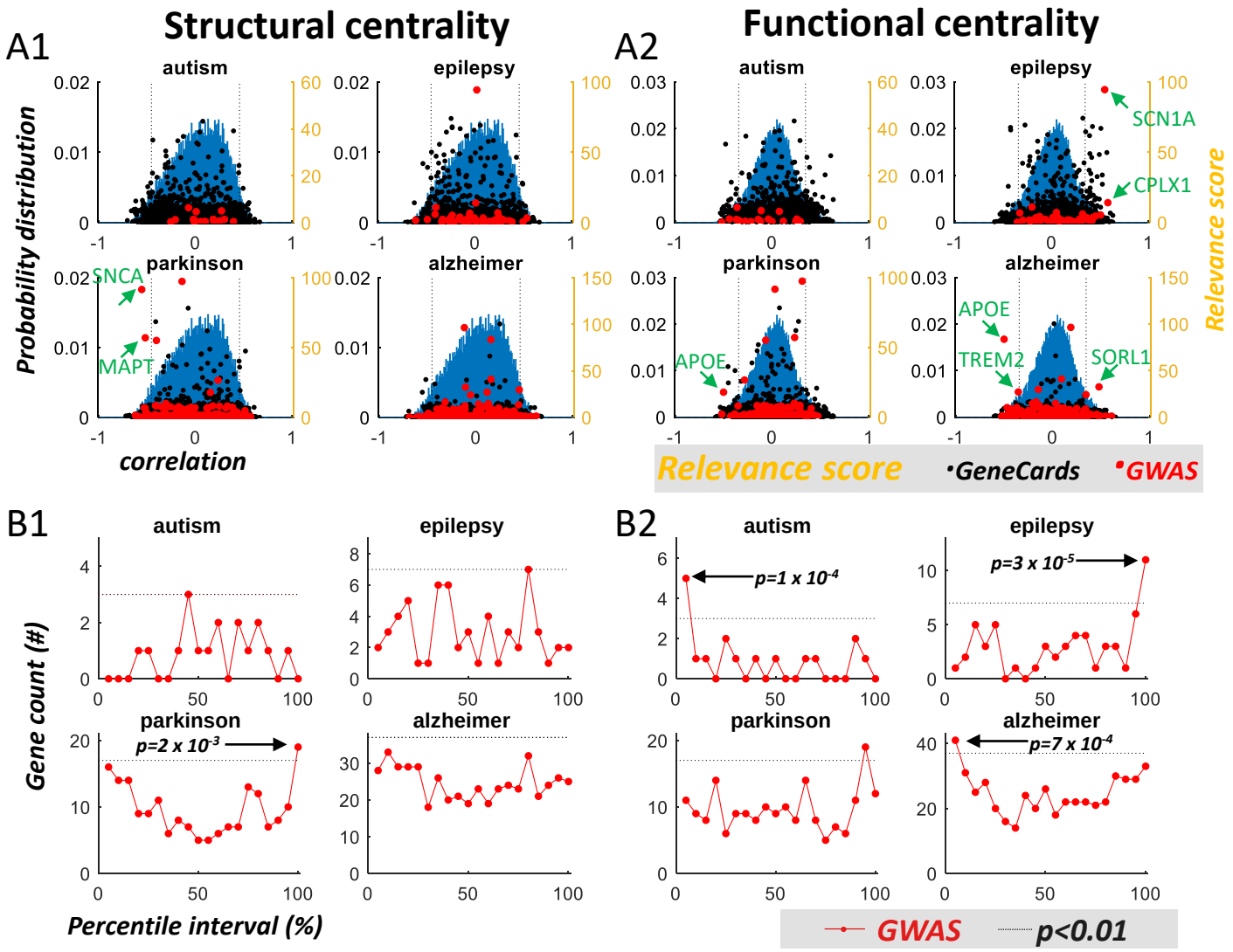
A1
Structural centrality
A2
Functional centrality
autism
epilepsy
parkinson
alzheimer
Probability distribution
Relevance score
SNCA
MAPT
SCN1A
CPLX1
APOE
TREM2
SORL1
correlation
Relevance score
GeneCards
GWAS
B1
B2
Gene count (#)
p=2 x 10-3
p=1 x 10-4
p=3 x 10-5
p=7 x 10-4
Percentile interval (%)
GWAS
p<0.01